PROCEEDINGS OF SCIENCE

PoS(ICRC2025)1121

Probing the Firn Refractive Index Profile Using Antenna Response

---

The RNO-G Collaboration
(a complete list of authors can be found at the end of the proceedings)

E-mail: `curtis.mclennan@ku.edu`, `zedlam@ku.edu`

We present a novel methodology for extracting firn ice properties using reflection coefficients ('S11') of antennas lowered into boreholes. Experiments like the Radio Neutrino Observatory in Greenland (RNO-G) require precise firn index of refraction profiles for accurate reconstruction of incident neutrinos and cosmic rays. Using a data-driven method guided by neutron probe measurements in the vicinity of Summit Station, a depth-dependent S11 profile can be translated into a refractive index profile. We present results based on data taken in August, 2024 and May, 2025 from boreholes at Summit Station, Greenland.

Corresponding authors: Curtis McLennan[1]*, Dave Besson[1]
[1] *University of Kansas*
* Presenter

39th International Cosmic Ray Conference (ICRC2025)
15–24 July 2025
Geneva, Switzerland

ICRC 2025
The Astroparticle Physics Conference
Geneva July 15-24, 2025

1. Introduction

Accurate and precise characterization of the radio-frequency (RF) response of glacial firn is essential for embedded UHEN experiments in Greenland and Antarctica seeking observation of neutrinos and cosmic rays using radio techniques. One parameter of particular interest is the ice index of refraction, which determines the speed of light in different media and dictates the detailed propagation of radio in firn ice. Thus far, this has been estimated by measuring the ice density profile with depth (ρ_{ice}(z)) and assuming a linear variation of refractive index with density [1, 2]. Simple measurements of mass per unit volume of ice cores, at ~1-m intervals, provide direct ρ(z) data, ignoring any possible perturbation to the ice during the drilling. Alternatively, after a core has been extracted, ρ(z) of the surrounding ice can be determined from neutron flux back-scattering via neutron probe monitors lowered on a winch. Herein, we describe an alternative procedure for determining n(z), requiring only an antenna, low-loss coaxial cable and a portable vector network analyzer (VNA).

Since radio antennas have well-understood properties that depend, in part, on their environment, multi-year measurements of antennas in a single borehole can be used to extract a local index of refraction profile by translating measured changes in antenna response into the properties of the local antenna ice environment.

2. Dataset and Processing

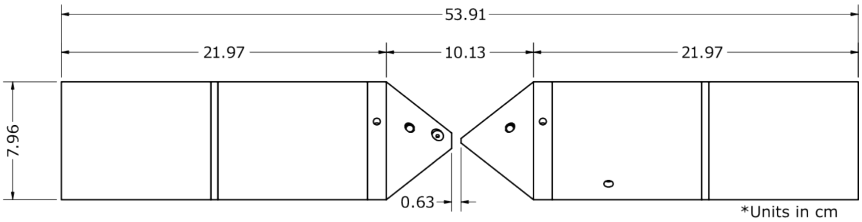

Figure 1: KU-VPol antenna schematic. An N-connectorized FLC12-50J cable is threaded through the left cylindrical chamber to the feedpoint.

A 350 m deep, 97 mm diameter ice hole drilled by the Ice Drilling Program (IDP, based at UW, Madison) during the summer of 2024 at Summit Station, Greenland, provided an opportunity to collect antenna impedance data, as a function of depth. In August, 2024, and again in May, 2025 we deployed a vertically polarized antenna (VPol) constructed at the University of Kansas (KU) based on the previous design of equipment used for 2018 transmitter measurements taken at the South Pole Ice Core Experiment (SPICE) borehole (Fig. 1). In 2024, the antenna response was measured to a depth of 100 m using a GV530 winch to lower the antenna, with uncertainty less than 1 cm (with no observed hysteresis). In 2025 the antenna was lowered by hand to a depth of 85.5 m with an estimated uncertainty of 10 cm. In both cases, complex reflection coefficient data were collected using a handheld FieldFox N9913B vector network analyzer (VNA). The full set of data-taking parameters for the two years is summarized in Tab.1. Spacers introduced in 2025 address the dominant uncertainty in the 2024 data analysis arising from unknown axial alignment [3]. A lower-loss coaxial cable along with VNA sweep averaging minimizes allows the higher-frequency

$\frac{3L}{2}$ resonance to be observed (L here designates the length of the antenna), in addition to the $\frac{L}{2}$ fundamental. For the 2025 dataset, measurements were taken as the antenna was raised, in addition to when it was lowered, providing two 'independent' data samples.

	2024	2025
N_{avg}	1	16
cable	120-m LMR-400	30-m LMR-600 + 2×30-m LDF4-50A
drop	GV530	lower by hand
σ_z	1 cm	10 cm
VNA P_{out}	-15 dBm	0 dBm
Air Temp	-8 C	-25 C
$S_{11,air}$	1 reference	several measurements
z_{min}	-100 m	-85.5 m
Axial alignment	no spacers	endcap spacers
Data Taking	↓ only	↓ and ↑

Table 1: Data-taking parameters for the 2024 and 2025 datasets.

Although we seek an exclusively data-driven analysis, we also have previously used the antenna modeling software HFSS in the Ansys Electromagnetics Suite 2023 R1 to simulate an axially oriented antenna in an evacuated borehole, immersed in firn, as an alternative analysis method in previous work [3]. The analysis presented here does not utilize simulation results.

2.1 Glacial Ice Properties

Ice properties change with depth, as the firn gradually compacts with increasing overburden. A linear dependence of local refractive index on local ice density [1, 2] is commonly assumed, allowing an estimate of n(z) from ρ(z) measurements. Since a changing index of refraction, by Fermat's Principle, results in curved, rather than rectilinear RF ray trajectories, it is essential to understand the index of refraction profile where these instruments have been deployed in order to reconstruct the geometry of neutrino interactions. Previous work has been done on the index of refraction profile by both the astroparticle [4] and glaciological communities [5, 6].

Unlike the Earth's atmosphere, which readily lends itself to a fluid density profile compressing under its own weight, compactification of accumulated snow proceeds through multiple phase transitions, often demarcated by two separate inflection points [6–8]. Snow is broadly defined as material that has not undergone change since deposition, while firn is under some form of transformation from snow to ice. A depth of $\sim$ 15 m – 20 m, marks stage 1 densification of firn, characterized by grain settling and packing. At a depth of ~80 m, firn ice transforms to 'bubbly ice', beyond which the ice structure is relatively constant, modulo a diminishing fraction of air inclusions.

2.2 Antenna Response In-Media

Antennas emit/receive electromagnetic radiation, converting the emitted/captured energy from/to electrical currents. The frequency bandwidth over which an antenna responds depends on antenna construction and geometry. For a half-wave dipole, the peak response ('resonance'), corresponding to maximal current magnitude, is typically obtained at a frequency $f = c/2L$, with L the characteristic length scale of the antenna itself. The antenna used in this work has two such in-air resonances in the frequency band of interest, one at ~ 200 MHz and another at ~ 600 MHz.

Antennas have inductive, capacitive, and resistive characteristics, which determine their complex impedance Z_L at each frequency. The mismatch between the impedance of an antenna and the impedance of the input/output at the feed determines how well it will radiate/respond at a frequency. The (complex) 'reflection coefficient' Γ is the ratio of the amplitude of the reflected wave and the incident wave in an antenna, providing a measure of the frequency-dependent antenna response. Γ is defined as

$$\Gamma = \frac{Z_L - Z_0}{Z_L + Z_0}, \tag{1}$$

where Z_L is the (complex) antenna input impedance, and Z_0 is the transmission line impedance (usually 50Ω and purely real). The magnitude of the reflection coefficient is related to the antenna $|S_{11}|$ parameter via:

$$|S_{11}|(dB) = 20\ln(|\Gamma|). \tag{2}$$

$|S_{11}| = 0$ dB corresponds to complete power reflection and therefore zero transmission; conversely, $|S_{11}| \to -\infty$ dB corresponds to perfect transmission at a given frequency. For the remainder of this article we will use 'S_{11}' to designate the magnitude of the $|S_{11}|$ parameter (rather than the complex value).

A medium can be characterized by its relative permittivity ϵ_r, relative permeability μ_r, and conductivity σ. The speed of electromagnetic waves in a medium is given by the familiar $v = c/n$, where c is the speed of light in vacuum and the refractive index $n = \sqrt{\epsilon_r}$. The *in situ* media impedance Z therefore scales inversely with frequency, via:

$$Z = \sqrt{\frac{\mu}{\epsilon}} = \sqrt{\frac{\mu_o \mu_r}{\epsilon_0 \epsilon_r}} = Z_v \sqrt{\frac{1}{\epsilon_r}} = \frac{Z_v}{n} \tag{3}$$

where μ_0 is the relative permeability of the vacuum, ϵ_0 is the relative permittivity of vacuum, and Z_v is the free-space impedance. We assume that the media of interest is non-magnetic.

Since the resonant antenna wavelength of a dipole is fixed by geometry to be $(2n+1)L/2$ (n=integer), the *in situ* antenna resonant frequency scales linearly (up to a coefficient and a constant offset) with $1/n$ as $f_{res} \sim a/(b+n)$, with a and b constants that depend on the fine details of both the antenna construction as well as the borehole into which the antenna is lowered; these constants can be extracted from the data itself.

In our case, for which a vertically-oriented antenna is deployed into a dry borehole, the antenna is not completely embedded in a single medium. Instead, it is immersed in a medium with an effective index of refraction n_{eff}, which is a weighted combination of the $n \approx 1$ air in the borehole and n_{firn} of the surrounding ice, so $n_{\mathrm{air}} \leq n_{\mathrm{eff}} \leq n_{\mathrm{firn}}$. Additional secondary effects like temperature, moisture content, and impurities are assumed to be negligible for this measurement.

3. Methodology

In order to determine $n(z)$ we map the resonant frequency as a function of depth $f(z)$ and the index of refraction as a function of resonant frequency $n(f)$. The two 'resonant' frequencies of interest to

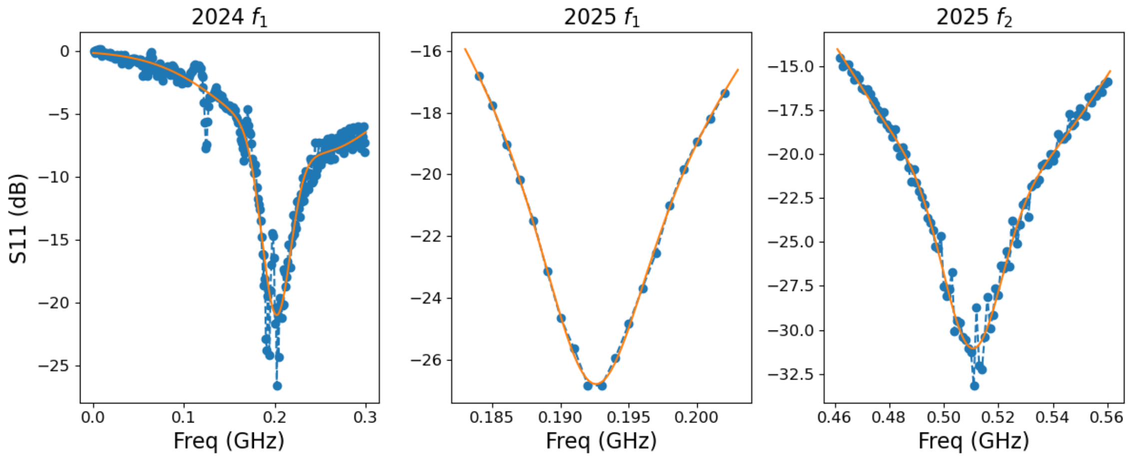

Figure 2: Example S_{11}(dB) fits taken at a depth of 13 m (selected arbitrarily). The 2024 f_1 and 2025 f_2 data are fitted using a double-Gaussian. The 2025 f_1 data is fitted using a double-Lorenztian.

us correspond to wavelengths $L/2$ (denoted f_1) and $3L/2$ (denoted f_2). We can extract, from data, the resonant frequency of the antenna as a function of depth $f_r(z)$, by fitting the S_{11}(f) distribution (in units of dB) at each depth to an appropriate functional form. In the case of the 2024 f_1 data as well as the 2025 f_2 data a double-Gaussian function was found to provide a satisfactory fit:

$$P(f) = A_1 \exp\left(\frac{-(f-\eta_1)^2}{2\sigma_1^2}\right) + A_2 \exp\left(\frac{-(f-\eta_2)^2}{2\sigma_2^2}\right) \tag{4}$$

with $A_{1,2}$ the amplitude of the Gaussian, $\eta_{1,2}$ the mean and $\sigma_{1,2}$ the standard deviation. For the 2025 f_1 data a double-Lorentzian was slightly preferred:

$$P(f) = \frac{A_1}{(f-\eta_1)^2 + \gamma_1^2} + \frac{A_2}{(f-\eta_2)^2 + \gamma_2^2} \tag{5}$$

where $A_{1,2}$ is the amplitude, $\eta_{1,2}$ is the peak position, and $\gamma_{1,2}$ is the width. An example fit of each type is shown in Fig. 2. Additional fitting schemes were examined (tracking the S_{11} minimum value, fitting to a double Lorentzian or a asymmetric Laplacian, e.g.) and found to yield similar results, though with less fitting stability and/or poorer convergence characteristics compared to the double Gaussian/Lorentzian.

Using both the double-Gaussian and the double-Lorentzian the minimum value of the fit was defined to be the resonant frequency for each dataset as a function of depth (Fig. 3); the typical deviation between the two functional forms was less than 1 MHz, corresponding to the binning of our S11 data. In the 2025 data there is a clear systematic reduction of the resonant values obtained during the (later) upwards-going (designated $f_\uparrow$), compared to the (earlier) downwards-going data ($f_\downarrow$) for both f_1 and f_2 shallower than 50 m. There are several possible causes for this discrepancy. In the field there was accumulated snow observed above and between each of of the endcap stabilizing fins when the antenna was raised up from the borehole after data-taking, presumably due to the antenna scraping the side of the borehole while being lowered/raised. This snow could affect the measured resonance by raising the effective refractive index around the antenna (by displacing air

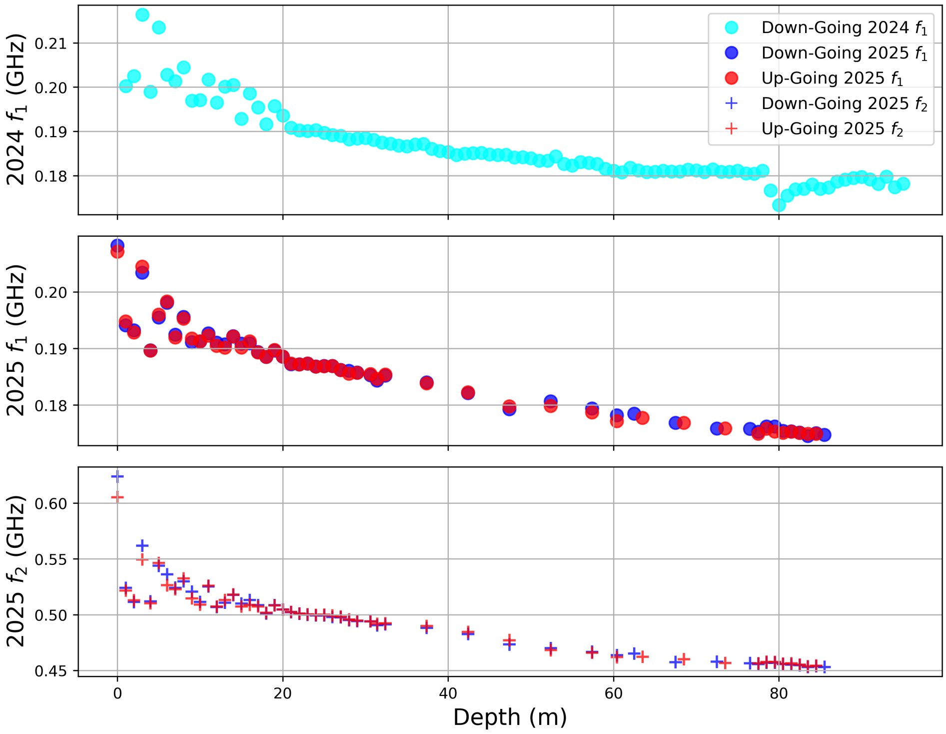

Figure 3: Extracted resonant frequencies for each data set plotted against depth.

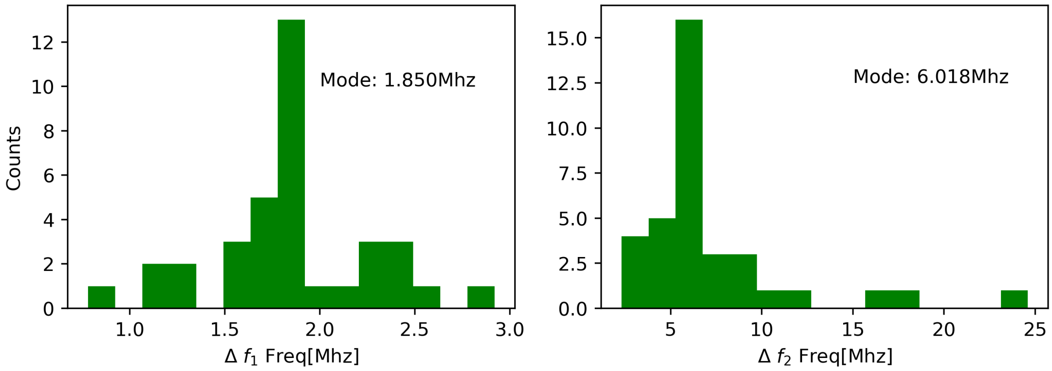

Figure 4: Difference of $(f_\uparrow)$ and $(f_\downarrow)$ for the 2025 f_1 and f_2 respectively. The mode bin is labeled.

with snow), resulting in a lower resonance value. Additionally, there could be VNA temperature dependence (expected to become more obvious with time), as the 2025 data were taken while the air temperature was -25 C. Both of these cases would bias later VNA readings towards lower values. We empirically correct for this by taking the mean of a distribution of $(f_\uparrow(z) - f_\downarrow(z))$ and applying that offset to the $f_\uparrow$ data (Fig. 4).

To determine $n(f_{1,2})$ for each dataset, we assume the physically-motivated functional form $f(n) = a/(b+n)$. The fundamental resonance of the antenna scales as $f_1 \sim c/(2\lambda_1)$ where λ_1 is the wavelength. However, λ_1 is our fixed antenna length. Therefore, since c scales as $1/n$ with

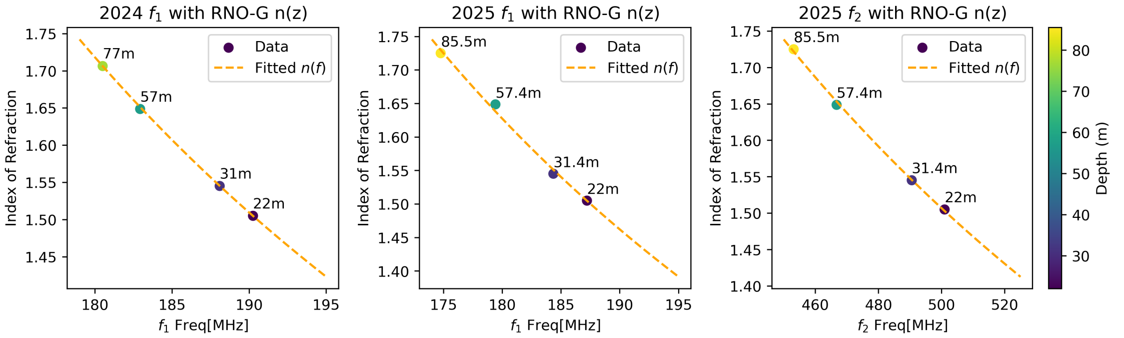

Figure 5: Form of $n(f)$ for all three datasets. The refractive index for each depth is determined from the fit described in [9], originating from neutron probe measurements.

a changing refractive index f_1 will also scale as $1/n$. To extract a and b, we plot the measured resonant frequencies against the refractive index derived from neutron probe density data, described in [9]. Four depths were chosen to fit to, 22 m as the shallowest point that does not display large density fluctuations. The deepest available depth, 85.5 m for 2025 data and 77 m for 2024 data (avoiding the bump starting at $\sim$ 80 m, which we can only, in retrospect, attribute to a data-taking anomaly). Additionally two arbitrary intermediate points 57 m and 31 m were included to reduce the dependence on our chosen points and to show the quality of the fit. Additionally, only data taken going down was used in the 2025 fits, allowing for the up-going data to be measured independently from fitting. We find that our ansatz gives a good match to the observed data (Fig. 5).

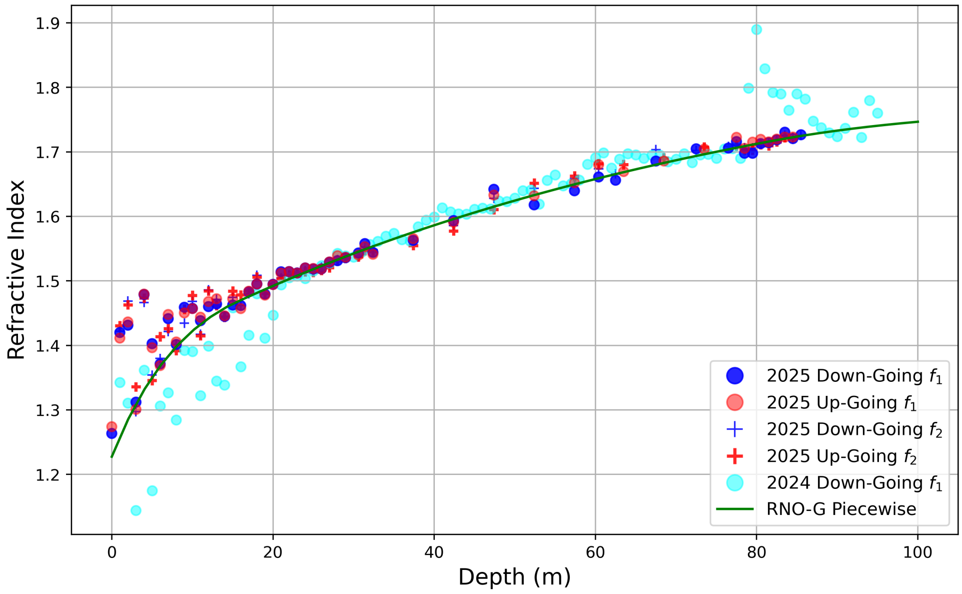

Figure 6: Overlaid $n(f(z))$ profiles for each dataset along with reference piecewise exponential found in [9].

However, by fitting to neutron probe measured (NPM) data the systematics affecting the NPM derived refractive index is highly correlated to systematics in our extracted refractive index profile. By combining the index of refraction as a function of resonant frequency $n(f)$ and the resonant frequency as a function of depth $f_r(z)$ from Summit data we obtain the $n(z)$ profile $n(f(z))$ shown in Fig. 6. We have worked to quantify the level of agreement between the 2024 and 2025 results. The conspicuous difference at 79 m – 85 m can be attributed as an artifact of certain systematics present in the 2024 data. This region showed anomalous response in the S_{11} curves, the cause of which has still to be identified. We have also attempted to quantify the possible correlation between the two datasets in the shallow region. This is complicated by snow accumulation and densification caused by heavy machinery present at the drill site. Nevertheless, a direct Pearson's correlation coefficient calculation returns a coefficient of .537 for the upper 29 m.

4. Conclusion

Understanding and quantifying ice properties such as the refractive index is important to polar UHEN experiments. We have shown that antenna response can be used to measure the index of refraction profile as a function of depth. This approach is advantageous owing to the ease of access to the requisite hardware components, which are 'standard' for current UHEN experiments. Our measurements yield results consistent with previous measurements of the refractive index at Summit Station. During the summer of 2025, the RNO-G experiment will work to systematically measure S_{11} for the 20 boreholes that will be drilled during the summer campaign; these measurements will be repeated during the summer of 2026 to inform estimates of local snow accumulation.

References

[1] V. Schytt *Geografiska Annaler* **40** no. 1, (1958) 85–87.

[2] A. Kovacs, A. J. Gow, and R. M. Morey *Cold Regions Science and Technology* **23** no. 3, (1995) 245–256.

[3] S. Agarwal *et al.*, "Probing the firn refractive index profile and borehole closure using antenna response," 2025. `https://arxiv.org/abs/2504.03862`.

[4] C. Welling and The RNO-G Collaboration *The Cryosphere* **18** no. 7, (2024) 3433–3437.

[5] R. L. Hawley and E. M. Morris *Journal of Glaciology* **52** no. 179, (2006) 491–496.

[6] C. M. Stevens, V. Verjans, J. M. D. Lundin, E. C. Kahle, A. N. Horlings, B. I. Horlings, and E. D. Waddington *Geoscientific Model Development* **13** no. 9, (2020) 4355–4377.

[7] M. M. Herron and C. C. Langway *Journal of Glaciology* **25** (1980) 373 – 385.

[8] A. N. Salamatin, V. Y. Lipenkov, and P. Duval *Journal of Glaciology* **43** no. 145, (1997) 387–396.

[9] P. Windischhofer *PoS* **ARENA2024** (2024) 003.

Full Author List: RNO-G (June 30th, 2025)

S. Agarwal[1], J. A. Aguilar[2], N. Alden[3], S. Ali[1], P. Allison[4], M. Betts[5], D. Besson[1], A. Bishop[6], O. Botner[7], S. Bouma[8], S. Buitink[9,10], R. Camphyn[2], J. Chan[6], S. Chiche[2], B. A. Clark[11], A. Coleman[7], K. Couberly[1], S. de Kockere[12], K. D. de Vries[12], C. Deaconu[3], P. Giri[13], C. Glaser[7], T. Glüsenkamp[7], H. Gui[4], A. Hallgren[7], S. Hallmann[14,8], J. C. Hanson[15], K. Helbing[16], B. Hendricks[5], J. Henrichs[14,8], N. Heyer[7], C. Hornhuber[1], E. Huesca Santiago[14], K. Hughes[4], A. Jaitly[14,8], T. Karg[14], A. Karle[6], J. L. Kelley[6], C. Kopper[8], M. Korntheuer[2,12], M. Kowalski[14,17], I. Kravchenko[13], R. Krebs[5], M. Kugelmeier[6], R. Lahmann[8], C.-H. Liu[13], M. J. Marsee[18], C. McLennan[1], K. Mulrey[10], M. Muzio[6,5], A. Nelles[14,8], A. Novikov[19], A. Nozdrina[4], E. Oberla[3], B. Oeyen[20], N. Punsuebsay[19], L. Pyras[14,21], M. Ravn[7], A. Rifaie[16], D. Ryckbosch[20], F. Schlüter[2], O. Scholten[12,22], D. Seckel[19], M. F. H. Seikh[1], Z. S. Selcuk[14,8], J. Stachurska[20], J. Stoffels[12], S. Toscano[2], D. Tosi[6], J. Tutt[5], D. J. Van Den Broeck[12,9], N. van Eijndhoven[12], A. G. Vieregg[3], A. Vijai[11], C. Welling[3], D. R. Williams[18], P. Windischhofer[3], S. Wissel[5], R. Young[1], A. Zink[8]

[1] University of Kansas, Dept. of Physics and Astronomy, Lawrence, KS 66045, USA
[2] Université Libre de Bruxelles, Science Faculty CP230, B-1050 Brussels, Belgium
[3] Dept. of Physics, Dept. of Astronomy & Astrophysics, Enrico Fermi Inst., Kavli Inst. for Cosmological Physics, University of Chicago, Chicago, IL 60637, USA
[4] Dept. of Physics, Center for Cosmology and AstroParticle Physics, Ohio State University, Columbus, OH 43210, USA
[5] Dept. of Physics, Dept. of Astronomy & Astrophysics, Center for Multimessenger Astrophysics, Institute of Gravitation and the Cosmos, Pennsylvania State University, University Park, PA 16802, USA
[6] Wisconsin IceCube Particle Astrophysics Center (WIPAC) and Dept. of Physics, University of Wisconsin-Madison, Madison, WI 53703, USA
[7] Uppsala University, Dept. of Physics and Astronomy, Uppsala, SE-752 37, Sweden
[8] Erlangen Centre for Astroparticle Physics (ECAP), Friedrich-Alexander-University Erlangen-Nürnberg, 91058 Erlangen, Germany
[9] Vrije Universiteit Brussel, Astrophysical Institute, Pleinlaan 2, 1050 Brussels, Belgium
[10] Dept. of Astrophysics/IMAPP, Radboud University, PO Box 9010, 6500 GL, The Netherlands
[11] Department of Physics, University of Maryland, College Park, MD 20742, USA
[12] Vrije Universiteit Brussel, Dienst ELEM, B-1050 Brussels, Belgium
[13] Dept. of Physics and Astronomy, Univ. of Nebraska-Lincoln, NE, 68588, USA
[14] Deutsches Elektronen-Synchrotron DESY, Platanenallee 6, 15738 Zeuthen, Germany
[15] Whittier College, Whittier, CA 90602, USA
[16] Dept. of Physics, University of Wuppertal D-42119 Wuppertal, Germany
[17] Institut für Physik, Humboldt-Universität zu Berlin, 12489 Berlin, Germany
[18] Dept. of Physics and Astronomy, University of Alabama, Tuscaloosa, AL 35487, USA
[19] Dept. of Physics and Astronomy, University of Delaware, Newark, DE 19716, USA
[20] Ghent University, Dept. of Physics and Astronomy, B-9000 Gent, Belgium
[21] Department of Physics and Astronomy, University of Utah, Salt Lake City, UT 84112, USA
[22] Kapteyn Institute, University of Groningen, PO Box 800, 9700 AV, The Netherlands

Acknowledgments

We are thankful to the support staff at Summit Station for making RNO-G possible. We also acknowledge our colleagues from the British Antarctic Survey for building and operating the BigRAID drill for our project.

We would like to acknowledge our home institutions and funding agencies for supporting the RNO-G work; in particular the Belgian Funds for Scientific Research (FRS-FNRS and FWO) and the FWO programme for International Research Infrastructure (IRI), the National Science Foundation (NSF Award IDs 2112352, 2111232, 2111410, 2411590, and collaborative awards 2310122 through 2310129), and the IceCube EPSCoR Initiative (Award ID 2019597), the Helmholtz Association, the Swedish Research Council (VR, Grant 2021-05449 and 2021-00158), the University of Chicago Research Computing Center, and the European Union under the European Unions Horizon 2020 research and innovation programme (grant agreements No 805486), as well as (ERC, Pro-RNO-G No 101115122 and NuRadioOpt No 101116890).